nature electronics

Article

https://doi.org/10.1038/s41928-025-01474-3

Direct bonding and debonding of two-dimensional semiconductors

Received: 29 July 2024

Accepted: 9 September 2025

Published online: 27 October 2025

Check for updates

Jieying Liu[1,2,7], Jiaojiao Zhao[1,2,3,7], Tong Li[1,4,7], Depeng Ji[1], Liyan Dai[2], Lu Li[2,3], Zheng Wei[2], JiaWei Li[2], Qinqin Wang[2], Hua Yu[1], Lanying Zhou[1], Yutong Chen[1], Fanfan Wu[2,3], Mingtong Zhu[2], Huacong Sun[2], Yun Li[1], Songge Zhang[1], Jinpeng Tian[2], Xingchao Zhang[1], Nianpeng Lu[2], Xuedong Bai[2], Zexian Cao[2], Shenghuang Lin[1], Shuopei Wang[1], Dongxia Shi[2,3], Na Li[1], Luojun Du[2,3], Wei Yang[2,3], LeDe Xian[5,6] & Guangyu Zhang[1,2,3]

Two-dimensional (2D) semiconductors are promising building blocks for advanced electronic devices. However, the fabrication of high-quality 2D semiconductor wafers with engineered layers remains a challenge. Here we describe a direct wafer bonding and debonding method that can be applied to semiconductor monolayers that have been grown epitaxially on high-adhesion substrates such as sapphire. The process operates in both vacuum and a glovebox environment and requires no intermediate-layer assistance. It produces stacked 2D semiconductors with clean interfaces and wafer-scale uniformity and allows precise control of layer numbers and the interlayer twist angle. We use the approach to create different homostructures and heterostructures with 2D monolayers, including molybdenum disulfide (MoS_2) and molybdenum diselenide ($MoSe_2$). We also show that the approach can directly bond monolayer MoS_2 onto high-κ dielectric substrates (HfO_2 and Al_2O_3) while preserving its intrinsic electronic properties.

Two-dimensional (2D) semiconductors are promising materials for making advanced electronic devices, including highly scaled integrated circuits. In the past decade, there have been several important demonstrations of both prototype devices and small-scale integrated circuits using 2D semiconductors[1–10]. To fully realize their potential, it is necessary to fabricate high-quality 2D semiconductors with engineered layers at the wafer scale, which can readily be achieved for molybdenum disulfide (MoS_2) through epitaxy[11–17]. However, due to lattice matching and thermodynamic limitations, this is applicable only to homostructures on certain substrates like sapphire, and the maximum thickness is limited to trilayers with a strictly aligned interlayer lattice orientation.

Previously, a transfer-and-stack route has been reported as a possible route to producing customized 2D semiconductor homostructures and heterostructures at wafer scale[18,19]. This route involves picking up individual 2D semiconductor layers from their growth substrates, transferring them to a target substrate and stacking them layer by layer. Typically, an adhesive polymer is used in the picking-up process as an intermediate layer. Unfortunately, the picking-up can be applied only to polycrystalline 2D semiconductors with low adhesion to their substrates (for example, monolayer MoS_2 on SiO_2) and fails for epitaxial 2D semiconductors with strong adhesion to their substrates (for example, MoS_2 on sapphire; see Supplementary Note 1 and Supplementary Fig. 1 for more details). In addition, the removal of the intermediate layer by

[1]Songshan Lake Materials Laboratory, Dongguan, China. [2]Beijing National Laboratory for Condensed Matter Physics and Institute of Physics, Chinese Academy of Sciences, Beijing, China. [3]School of Physical Sciences, University of Chinese Academy of Sciences, Beijing, China. [4]School of Physics and Electronics, Hunan University, Changsha, China. [5]Tsientang Institute for Advanced Study, Hangzhou, China. [6]Max Planck Institute for the Structure and Dynamics of Matter, Center for Free-Electron Laser Science (CFEL), Hamburg, Germany. [7]These authors contributed equally: Jieying Liu, Jiaojiao Zhao, Tong Li. e-mail: gyzhang@iphy.ac.cn

https://doi.org/10.1038/s41928-025-01474-3

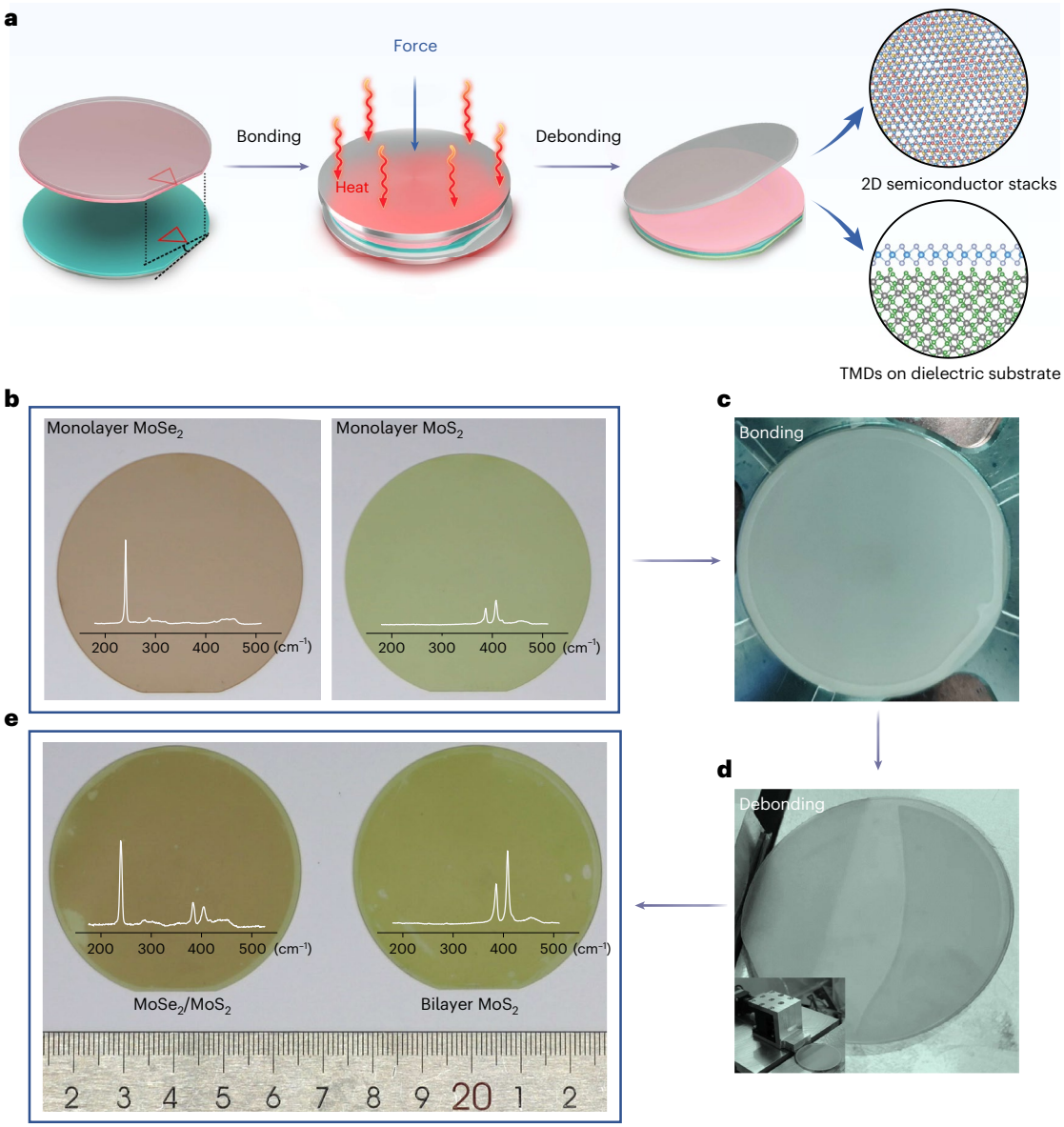

Fig. 1 | Wafer-scale transfer of 2D materials by bonding–debonding. **a**, Schematic illustration of the bonding and debonding process. **b**, Photographs of a 2-inch monolayer $MoSe_2$ wafer (left) and a monolayer MoS_2 wafer (right). Insets: Corresponding Raman spectra. **c**,**d**, Photographs of a wafer pair after bonding (**c**) and during debonding (**d**). The inset in **d** shows the debonding set-up. **e**, Photographs of a 2-inch $MoSe_2/MoS_2$ heterostructure wafer (left) and a bilayer MoS_2 wafer (right) obtained through the bonding–debonding technology. Insets: Corresponding Raman spectra. TMD, transition-metal dichalcogenide.

wet-etching or dissolving adds further post-processing and cleaning steps and can cause structural damage or contamination of the surface and interface, which is an important source of quality degradation.

In this Article, we report a direct bonding–debonding method for creating layer-engineered 2D semiconductor wafers by manipulating high-quality monolayer 2D semiconductors epitaxially grown on sapphire. Direct bonding is achieved without an intermediate layer. Two target wafers are placed face to face in a high-vacuum wafer-bonding system, where a twist offset can be introduced, to create ultraclean homostacks or heterostacks with an interlayer twist angle variation under ±1°. Then, wafer debonding from the sapphire substrate is achieved by mechanical peeling using a double cantilever set-up designed to minimize the critical energy release rate and achieve crack-free debonding. We show our method can be used to create bilayer MoS_2, $MoSe_2/MoS_2$ heterostructure and trilayer MoS_2 using 2-inch wafer monolayers. Direct bonding–debonding can also be used to transfer monolayer MoS_2 from sapphire to high-κ substrates such as hafnium oxide (HfO_2). The direct bonding–debonding technique is compatible with mainstream semiconductor fabrication processes.

Direct wafer bonding of monolayer 2D semiconductors

Wafer bonding is a standard and widely adopted process in silicon manufacturing lines for heterogeneous integrations[20,21]. For direct wafer bonding without the assistance of any intermediate layers, the surface flatness is crucial when joining two rigid wafers. Full atomic contact is desired for stable bonding, yet it is extremely difficult to realize for conventional semiconductors and metals, even after polishing[22]. In comparison, the atomic flat surfaces of 2D semiconductors make it easier to form full atomic contact during bonding (refer to Supplementary Note 2 and Supplementary Figs. 2 and 3 for more details). Figure 1a illustrates the bonding and debonding process of two monolayer semiconductor wafers. The starting samples used in this work for bonding and debonding are 2-inch wafers of monolayer

https://doi.org/10.1038/s41928-025-01474-3

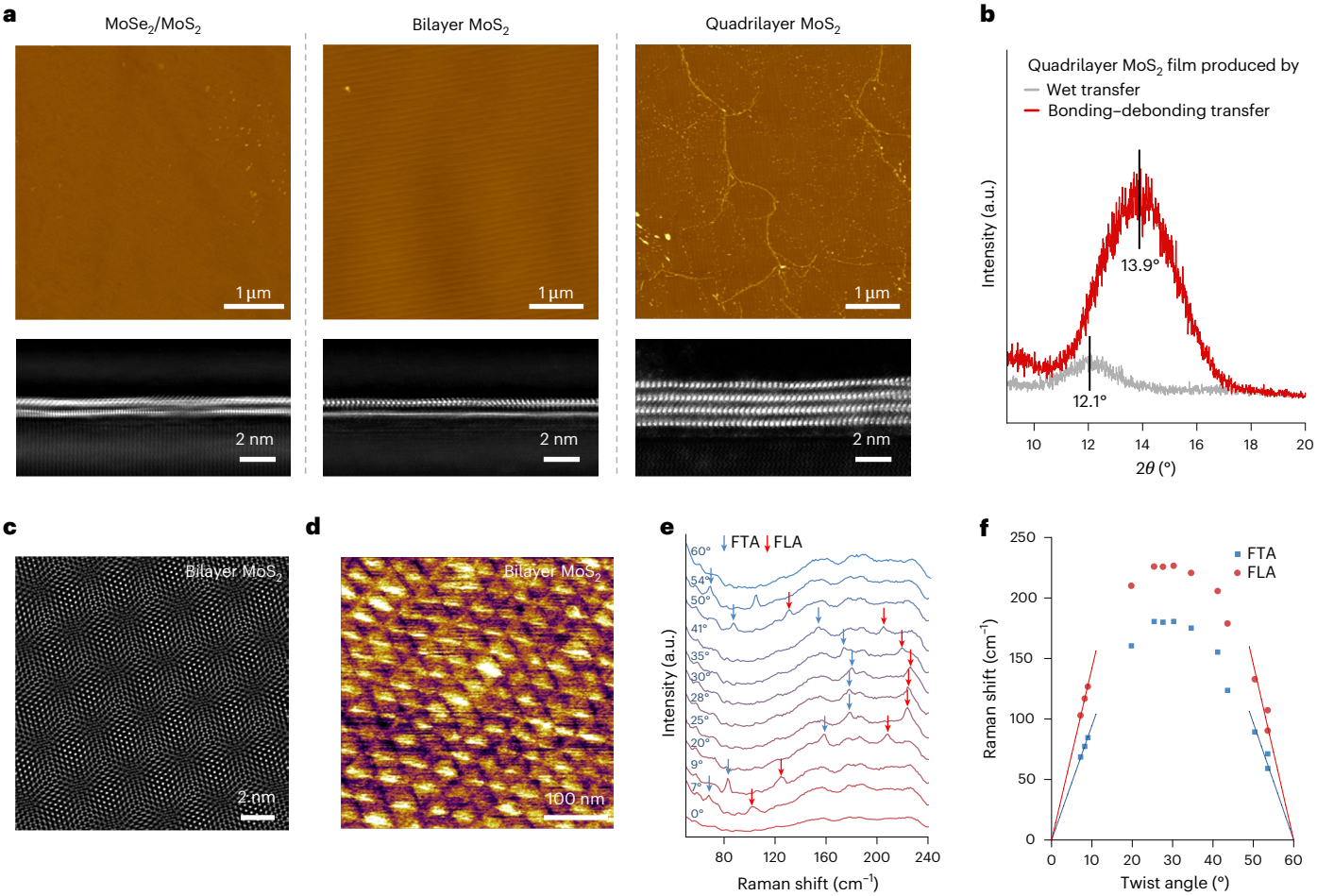

Fig. 2 | Clean surfaces and interfaces of stacked 2D materials obtained by bonding–debonding. a, AFM images (first row) and cross-sectional STEM band-pass-filtered images (second row) of $MoSe_2/MoS_2$ (left), bilayer MoS_2 (middle) and quadrilayer MoS_2 (right) prepared by bonding–debonding. Height scales: ±5 nm. **b**, Out-of-plane XRD pattern of quadrilayer MoS_2 films produced by wet transfer (grey) and bonding–debonding (red). **c**, STEM band-pass-filtered image of tBLMs with a twist angle of 5.3°. **d**, PFM image of tBLMs with a twist angle of 0.8°. **e**, Moiré phonons in tBLMs with different twist angles. **f**, Twist-angle-dependent frequencies of FTA and FLA modes extracted from **e**.

semiconductors (for example, MoS_2 and $MoSe_2$) epitaxially grown on c-plane sapphire, as illustrated in Fig. 1b. These epitaxial monolayer semiconductors on sapphire are fully covered, ultraflat with surface roughness below 0.14 nm (mainly originating from the surface steps of sapphire; Supplementary Fig. 2) and highly oriented with their $[10\bar{1}0]$ direction aligned to the $[11\bar{2}0]$ direction of the sapphire[11,23]. During the direct bonding process, two wafers (top and bottom) are first loaded face to face into a high-vacuum wafer-bonding system with a preset twist angle (θ). The two loaded wafers are then annealed at ~70 °C in vacuum for ~2 h for surface cleaning. Then, the two wafers are heated up to 120 °C and brought into contact with a press force of ~8,000 N. Complete bonding takes 5 min. An example of a bonded wafer pair is shown in Fig. 1c.

Debonding of bonded 2D bilayers

For the debonding of 2D bilayers from one of two sapphire substrates, we designed a debonding set-up, as shown in the inset of Fig. 1d. The set-up is equipped with a steel blade (which can move up and down with a tunable loading rate) and a sample stage (whose temperature can be controlled in the range from room temperature to 400 °C). Mechanical peeling uses a double cantilever beam configuration[24,25]. See Supplementary Note 3 and Supplementary Video 1 for more details. Note that, in previous methods for the mechanical exfoliation of 2D layers from their substrates by flexible cantilevers, cracks and holes frequently appear in the exfoliated 2D materials because of uncontrolled deformation and considerable mechanical stress[26,27]. By contrast, both cantilevers in the present case are rigid sapphire with a Young's modulus of ~370 GPa. As a result, the deformation and stress exerted on the 2D materials can be controlled and restricted to a very low level.

During the debonding process, the critical energy release rate (G_c) of the cracked interface is important. In interface fracture mechanics, a smaller G_c is more favourable for stable and crack-free peeling. As a lower loading rate and higher temperature lead to smaller G_c (refs. 24,25,28–32), we chose a sample stage temperature of 90 °C and loading rate of 2 μm s^{-1} for our debonding experiments, unless otherwise noted. See also the control experiments illustrated in Supplementary Figs. 4 and 5 for more details.

Regarding the bonded wafer pair, three van der Waals interfaces are formed (Extended Data Fig. 1): S1–L1, L1–L2 and L2–S2, where S denotes the sapphire substrate and L denotes the 2D semiconductor layer. Generally, mechanical peeling occurs at the interface with the lowest adhesion energy (E). For bonded MoS_2–$MoSe_2$ (heterobonding), as $E_{MoSe_2-sapphire} < E_{MoS_2-sapphire} < E_{MoSe_2-MoS_2}$, debonding occurs at the interface between $MoSe_2$ and sapphire. See Supplementary Notes 4 and 5 (Supplementary Figs. 6–8) for more details. Figure 1e (left) and Extended Data Fig. 2a show two typical wafers after debonding. The $MoSe_2$ monolayer is almost completely peeled off from the sapphire substrate and still bonded with the MoS_2 monolayer to form

https://doi.org/10.1038/s41928-025-01474-3

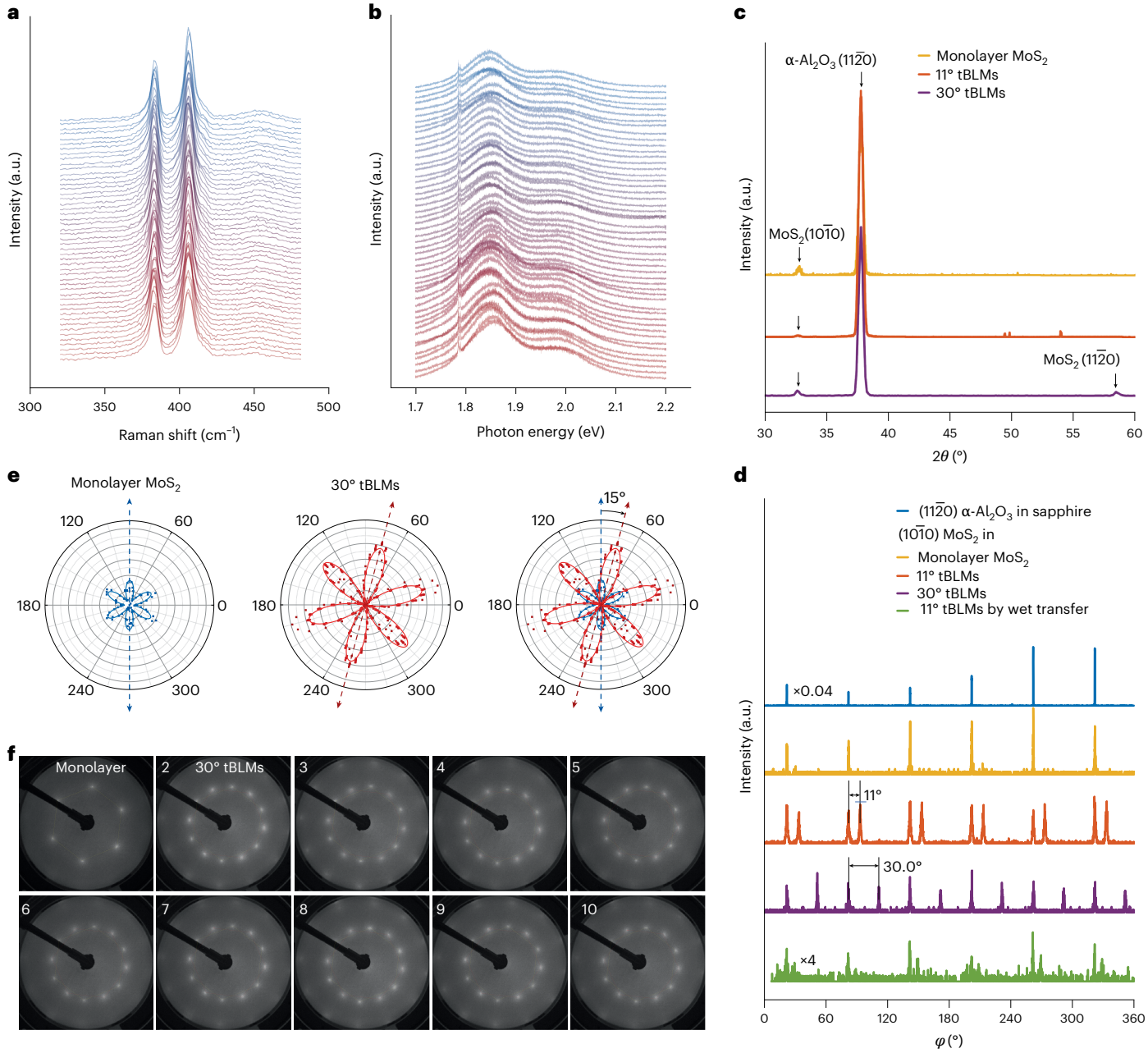

Fig. 3 | Wafer-scale uniformity of optical properties and twist angles. **a**,**b**, Raman (**a**) and PL (**b**) spectra collected from 50 different locations on a 2-inch 30° tBLMs wafer. **c**, In-plane XRD 2θ scan of monolayer MoS_2 (yellow), 11° tBLMs (orange) and 30° tBLMs (purple) produced by bonding–debonding. **d**, In-plane XRD φ scan of the (11$\bar{2}$0) plane of α-Al_2O_3 in monolayer MoS_2 (blue), (10$\bar{1}$0) plane of MoS_2 in monolayer MoS_2 (yellow), in 11° tBLMs (orange) and 30° tBLMs (purple) produced by bonding–debonding and in 11° tBLMs produced by the wet-transfer method (green). **e**, Polar plots of the SHG intensity of a 30° tBLMs film in a monolayer area (left) and several locations in a bilayer area (middle). Solid lines are the fitting results. The 15° angle between SHG petals (right) indicates that the twist angle between two MoS_2 layers is 30°. **f**, LEED patterns of a 30° tBLMs wafer probed at nine different locations.

a $MoSe_2$/MoS_2 bilayer on sapphire. The transfer yield calculated from a contrast-enhanced photograph is >92% (inset of Extended Data Fig. 2a), and the failed area mainly lies on the wafer edge due to the incomplete contact during wafer bonding. The near complete transfer of the $MoSe_2$ layer is also confirmed from Raman spectra characterizations (Extended Data Fig. 2d–i) and direct photoluminescence (PL) imaging (Supplementary Fig. 9).

For MoS_2–MoS_2 bonding (homo-bonding), as $E_{MoS_2-sapphire}$ is the same in both wafers, debonding would occur at both the S1–L1 and L2–S2 interfaces, leading to an unstable peeling process and fragmented MoS_2 bilayers on both sapphire surfaces (Extended Data Fig. 3c, left panel). To achieve the preferential peeling off from one of the sapphire substrates, we, thus, use a slightly domed pressing head in the bonding process to introduce differences in the peeling force between the two MoS_2–substrate interfaces. Consequently, debonding can be controlled to occur only at one MoS_2–sapphire interface. Refer to Supplementary Note 5 (Supplementary Fig. 8) and Extended Data Fig. 3 for more details. A typical as-obtained bilayer MoS_2 wafer is shown in Fig. 1e (right), with corresponding Raman characterizations (Extended Data Fig. 4) and optical microscopy images (Supplementary Fig. 10) validating the complete and intact transfer.

To demonstrate the universality and scalability of our bonding–debonding method, we also fabricated various other heterostructures, such as graphene/MoS_2/sapphire, WS_2/MoS_2/sapphire, MoS_2/$MoTe_2$/

https://doi.org/10.1038/s41928-025-01474-3

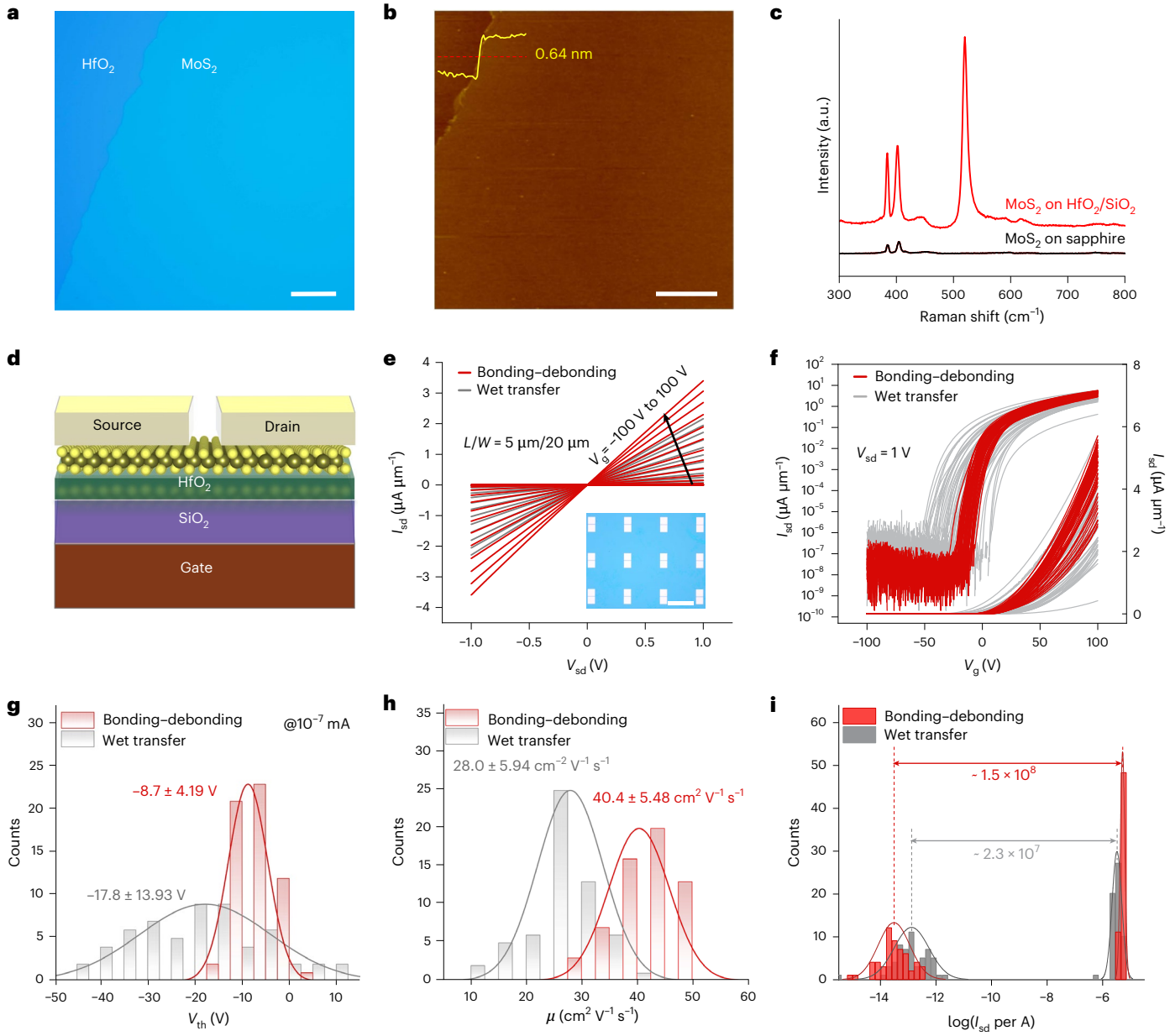

Fig. 4 | Transfer of MoS_2 from sapphire onto HfO_2. **a**, Optical microscopy image of MoS_2/HfO_2 produced by bonding–debonding. **b**, AFM image of MoS_2/HfO_2 produced by bonding–debonding. **c**, Raman spectra of monolayer MoS_2 film before (black) and after (red) transfer onto HfO_2. **d**, Schematic of an FET device made from monolayer MoS_2. **e**, Typical output curves of an FET device fabricated from MoS_2 transferred by bonding–debonding (red) and MoS_2 produced by wet transfer (grey). Inset: Optical microscopy image of FET device arrays. **f**, Transfer curves of 59 FET devices made from MoS_2 transferred by bonding–debonding (red) and 59 FET devices made from MoS_2 produced by wet transfer (grey). The left *y* axis is on a logarithmic scale, and the right *y* axis is on a linear scale. **g**–**i**, Statistical distribution of the threshold voltage V_{th} (**g**), mobility μ (**h**) and the on/off ratio (**i**) of 59 FET devices made from MoS_2 transferred by bonding–debonding (red) and 59 FET devices made from MoS_2 produced by wet transfer (grey). Scale bars, 50 μm (**a**), 3 μm (**b**), 400 μm (**e**, inset). I_{sd}, source–drain current density (I/W, where I is the source–drain current and W is the channel width); V_{sd}, source–drain voltage; V_g, gate voltage; L, channel length.

SiO_2 (Extended Data Fig. 5) and MoS_2/Au (Supplementary Fig. 11). Refer to Extended Data Fig. 6 and Fig. 2 for more details on the fabrication of trilayer and quadrilayer MoS_2 on sapphire.

Characterization of surface and interface quality

As direct wafer-to-wafer bonding is performed in a vacuum, no extra chemicals or other contamination sources are introduced. Consequently, the as-produced stacked 2D semiconductor wafers have ultraclean surfaces and interfaces. To confirm this, we performed atomic force microscopy (AFM), cross-sectional scanning transmission electron microscopy (STEM) and X-ray diffraction (XRD) characterizations.

Figure 2a (upper row) shows AFM topography images of the as-fabricated $MoSe_2/MoS_2$ bilayer, MoS_2 bilayer and MoS_2 quadrilayer made using our bonding–debonding method. In contrast to samples fabricated with the wet technique, which have dense bubbles and wrinkles across the sample, samples from the bonding–debonding method have atomically flat and clean surfaces and bubbles and wrinkles are rarely seen. Extended Data Fig. 7 shows corresponding controlled samples fabricated from a conventional wet-etching and transfer technique (see Methods for details). The cross-sectional STEM images of bonding–debonding samples in Fig. 2a (lower row) confirm the atomically sharp and ultraclean interfaces. Larger scale

images are shown in Supplementary Fig. 12a–c. Figure 2b shows the out-of-plane XRD patterns of quadrilayer MoS_2 fabricated by bonding–debonding (red line) and wet transfer (grey line). The 2θ scans of the bonding–debonding sample and wet-transferred sample peak at $2\theta = 13.9°$ and $2\theta = 12.1°$, corresponding to interlayer distances of 0.64 nm and 0.73 nm, respectively. The smaller interlayer spacing of 0.64 nm in the bonding–debonding samples is close to ~0.62 nm in natural MoS_2 crystals, validating that the stacking of bonded 2D layers is more compact.

Owing to the high interface and surface quality achieved by the bonding–debonding method, we could visualize the clear moiré superlattices in twisted bilayer MoS_2 (tBLMs) by both STEM (Fig. 2c and Supplementary Fig. 12d) and piezoelectric force microscopy (PFM) (Fig. 2d and Supplementary Fig. 13). In typical PL spectra (Extended Data Fig. 8b), intralayer MoS_2 A-exciton peaks (red arrows) and $MoSe_2$ A-exciton peaks (black arrows) in $MoSe_2/MoS_2$ and bilayer MoS_2 films are greatly suppressed with respect to those in the monolayers, indicating the strong interlayer coupling[33]. The intrinsic effects of twist angle on phonons, excitons and band structure are also identified. The periodic moiré potentials can be used to engineer the phonon dispersion and result in folded longitudinal acoustic (FLA) and folded transverse acoustic (FTA) phonons related to moiré phonons[34] (Fig. 2e). The relation between the twist angles and moiré phonon frequencies of FLA and FTA is summarized in Fig. 2f, showing a mirror behaviour either side of the twist angle of 30°. The corresponding PL characterizations in Extended Data Fig. 8 reveal a change in the optical indirect bandgap from 1.45 eV at $\theta = 0°$ and 1.60 eV at $\theta = 30°$ to 1.47 eV at $\theta = 60°$, consistent with previous results[35]. These characterizations confirm the high quality of the bonding–debonding samples.

Wafer-scale uniformity of twisted 2D semiconductors

In stacked van der Waals homostructures and heterostructures, the twist angle between adjacent layers has a crucial role in tuning properties such as superconductivity, correlated insulating states, ferroelectricity, ferromagnetism and moiré excitons[36–39]. However, previous studies were limited to the micrometre-scale, mainly due to the shortage of large-scale twisted samples. Our wafer-scale 2D semiconductor stacks with engineered twist angles fabricated by direct bonding–debonding provide ideal samples for large-scale investigations. We, thus, characterize the quality and uniformity of the as-fabricated wafer-scale twisted 2D semiconductors. Figure 3a (Fig. 3b) shows 50 representative room-temperature Raman (PL) spectra across a 2-inch 30° tBLMs wafer. The corresponding Raman mappings are shown in Extended Data Fig. 4g–h. Refer to Extended Data Fig. 2b,c,j–l for characterizations of a twisted $MoSe_2/MoS_2$ wafer. Both wafers exhibit uniform Raman and PL peak positions across the entire wafers, revealing the wafer-scale uniformity.

XRD, low-energy electron diffraction (LEED), second harmonic generation (SHG) and selected-area electron diffraction revealed the uniformity of the twist angle. Figure 3c (Fig. 3d) shows in-plane XRD θ–2θ (φ) scan of typical 11° and 30° tBLMs wafers produced by bonding–debonding[40]. Both MoS_2 $(10\bar{1}0)$ and the sapphire $(11\bar{2}0)$ peaks appear in the θ–2θ scan, indicating the aligned lattice between the first layer of MoS_2 and sapphire. For the 30° tBLMs, another MoS_2 $(11\bar{2}0)$ diffraction peak appears and comes from the second layer, as the zigzag direction in the second layer aligns with the armchair direction in the first layer. Figure 3d shows the in-plane φ-scan of sapphire $(11\bar{2}0)$ and MoS_2 $(10\bar{1}0)$ in 11° and 30° twisted wafers. Corresponding data on control samples of a monolayer MoS_2 and a 11° tBLMs fabricated by conventional wet transfer are also included. We can see that monolayer MoS_2 on sapphire exhibits six peaks due to the sixfold symmetry of MoS_2 $(10\bar{1}0)$ planes and sapphire $(11\bar{2}0)$ planes, whereas 11° (30°) twisted samples exhibit 12 peaks with adjacent peak separations of ~11° (~30°). By contrast, no recognizable second-layer peaks are seen in the wet-transferred tBLMs samples, most probably due to twist-angle inhomogeneity. Figure 3e shows polar charts for the measured polarization dependence of the SHG signals in the 30° tBLMs wafers. The uniform rotation of the petals by 15° confirms the 30° twist angle. Also see Supplementary Note 6 and Supplementary Fig. 14 for calculated SHG results. Figure 3f shows LEED patterns from nine randomly picked locations on the wafer, which again confirms the wafer-scale uniformity of the twist angles. The wafer-scale distribution of the twist angle was investigated by selected-area electron diffraction (Supplementary Fig. 15), finding a variation range of less than ±1°. These data substantiate the capability of our bonding–debonding method for wafer-scale, uniform and precise twist-angle control.

Direct bonding of monolayer MoS_2 to dielectric substrate

It has been suggested that the adhesion of the MoS_2/HfO_2 interface is higher than that of the MoS_2/Al_2O_3 interface[41]. We, thus, directly bonded epitaxial monolayer MoS_2 on sapphire onto bare dielectric substrates of HfO_2. Subsequently, we debonded the sapphire. In this way, we transferred the monolayer MoS_2 onto the HfO_2 surface. Figure 4a shows an optical microscopy image and Fig. 4b an AFM image of the monolayer MoS_2 on the HfO_2 after debonding. It can be seen that only a partial transfer was achieved, most probably due to the surface of the HfO_2 (grown on SiO_2 by atomic layer deposition) not being atomically flat (root mean square = 0.325 nm; Supplementary Fig. 16a) and, thus, not in full contact with the monolayer MoS_2. A zoom-in AFM image of the MoS_2 on the HfO_2 after bonding–debonding reveals an ultraflat (root mean square = 0.156 nm; Supplementary Fig. 16b) and wrinkle-free surface with monolayer thickness $t \approx 0.64$ nm. See Extended Data Figs. 9 and 10 for more characterizations. Supplementary Fig. 17 shows the monolayer MoS_2 directly bonded to the Al_2O_3 surface. The Raman spectra of monolayer MoS_2 films on sapphire and on HfO_2 in Fig. 4c, show no obvious peak shifts. Note that the enhanced phonon intensity for MoS_2 on the HfO_2/SiO_2 substrate is due to the effect of coherence enhancement.

The ultraflatness and cleanliness of the monolayer MoS_2 directly bonded onto HfO_2 are favourable for use in electronic devices. To confirm this, we fabricated and characterized field-effect transistors (FETs) with monolayer MoS_2 bonded onto HfO_2, as illustrated in the inset of Fig. 4e (see Methods for details). Similar FETs fabricated from monolayer MoS_2 wet-transferred onto HfO_2 are also included for comparisons. Transfer (output) curves from bonding–debonding devices and wet-transferred devices are plotted in Fig. 4f (Fig. 4e). Compared with FETs fabricated by the wet-transfer method, the FETs made by bonding–debonding show less device-to-device variations of the threshold voltage (V_{th}) (−8.7 ± 4.19 V versus −17.8 ± 13.93 V), higher mobility (40.4 ± 5.48 $cm^2 V^{-1} s^{-1}$ versus 28.0 ± 5.94 $cm^2 V^{-1} s^{-1}$) and higher on/off ratios (~1.5×10^8 versus ~2.3×10^7), as shown in Fig. 4g–i. The lower V_{th} variation, higher electron mobility and higher on-state current density in the bonding–debonding devices is attributed to the pristine interfaces obtained by the bonding–debonding process.

Conclusions

We have described a direct wafer bonding and debonding method for fabricating stacked 2D semiconductor wafers with engineered layer numbers and interlayer twist angles. The technology can be used to create 2D homostructures and heterostructures with clean surfaces and interfaces while controlling the twist angle of the stacks with high precision without affecting the wafer-scale uniformity and integrity of the materials. The technique can also be used to transfer 2D semiconductor films onto various dielectric substrates. Finally, the process is compatible with mainstream semiconductor fabrication processes. Our direct bonding–debonding method could facilitate both fundamental studies (for example, in twistronics) and the transition of 2D semiconductor-based integrated circuits from lab to fab.

Methods

2D semiconductor growth

The 2D semiconductors investigated in this work are wafer-scale monolayer MoS_2 and $MoSe_2$ epitaxially grown on c-face sapphire by oxygen-assisted chemical vapour deposition, as described in our previous works[12,13,23].

Bonding and debonding process

The wafter bonding process was performed in a commercial bonding system (EVG-510). During bonding, the vacuum pressure was kept at 3×10^{-5} Torr. After bonding, the wafers (as a whole) were transferred to a home-made debonding tool in a glovebox for debonding. During debonding, the temperature of the sample stage was set to 90 °C. For the graphene/MoS_2 heterobonding, the bonding was performed with a press force of 2,000 N at 180 °C for 10 min. For the bonding of monolayer MoS_2 onto a dielectric substrate, the bonding was performed using a domed pressing head at 180 °C for 30 min.

Wet-etching and transfer process

First, a poly(methyl methacrylate) (PMMA) film (5%, 950) was spin-coated onto MoS_2/sapphire for mechanical support. Then, we used a 1 mol l^{-1} potassium hydroxide (KOH) solution to etch away the sapphire substrate. We then transferred the MoS_2/PMMA film onto the target substrate. Finally, the PMMA film was removed using an acetone solution.

Material characterization

Raman and PL spectra were collected in ambient conditions by a Horiba LabRam HR Evolution Raman system with a 532-nm laser excitation. Direct PL images were acquired using a Leica STELLARIS 8 confocal microscope platform with an excitation wavelength of 532 nm. AFM and PFM imaging were performed by Asylum Research Cypher S instruments. Cross-sectional STEM images were recorded with a spherical aberration-corrected TEM (JEM-ARM200F) operating at 200 kV. Selected-area electron diffraction patterns were obtained using a field emission TEM (JEM-F200) operating at 200 kV. XRD was performed with an X-ray diffractometer (Rigaku SmartLabXE) with an in-plane adaptor. The angle between the sample surface and the X-ray incidence plane was 0.28°. LEED measurements were performed in a customized system (OCI BDL800IR-LMX-ISH) with a base pressure of $<8.9 \times 10^{-8}$ Pa and spot size of ~150 µm. SHG was performed in a customized system (MStarter 100-SHG) equipped with an ultrafast laser of wavelength 1,064 nm (Rainbow 1064 OEM). The accumulation time was 1 s, and the laser power was 10.4 mW.

Device fabrications and measurements

First, a standard ultraviolet-lithography process was used to pattern the source/drain contacts. Then, an electron beam was used to evaporate 2/30 nm Ti/Au contacts and for lift-off. Last, monolayer MoS_2 film was patterned into ribbons by ultraviolet lithography and oxygen reactive-ion etching. The electrical measurements were carried out in a probe station (Janis 4-probe station) with a base pressure of 10^{-6} Torr using a semiconductor parameter analyser (Agilent B1500).

Data availability

The datasets used for Figs. 1–4 and Extended Data Figs. 2, 4, 5, 8 and 9 are provided as source data. These datasets can be accessed via figshare at https://doi.org/10.6084/m9.figshare.30252058.v1 (ref. 42). All other data are available from the corresponding author upon request. Source data are available with this paper.

References

1. Liu, Y. et al. Promises and prospects of two-dimensional transistors. *Nature* **591**, 43–53 (2021).
2. Wang, S. et al. Two-dimensional devices and integration towards the silicon lines. *Nat. Mater.* **21**, 1225–1239 (2022).
3. Radisavljevic, B., Radenovic, A., Brivio, J., Giacometti, V. & Kis, A. Single-layer MoS_2 transistors. *Nat. Nanotechnol.* **6**, 147–150 (2011).
4. Desai, S. B. et al. MoS_2 transistors with 1-nanometer gate lengths. *Science* **354**, 99–102 (2016).
5. Wu, F. et al. Vertical MoS_2 transistors with sub-1-nm gate lengths. *Nature* **603**, 259–264 (2022).
6. Li, W. et al. Approaching the quantum limit in two-dimensional semiconductor contacts. *Nature* **613**, 274–279 (2023).
7. Migliato Marega, G. et al. Logic-in-memory based on an atomically thin semiconductor. *Nature* **587**, 72–77 (2020).
8. Li, N. et al. Large-scale flexible and transparent electronics based on monolayer molybdenum disulfide field-effect transistors. *Nat. Electron.* **3**, 711–717 (2020).
9. Tang, J. et al. Low power flexible monolayer MoS_2 integrated circuits. *Nat. Commun.* **14**, 3633 (2023).
10. Zhu, J. et al. Low-thermal-budget synthesis of monolayer molybdenum disulfide for silicon back-end-of-line integration on a 200 mm platform. *Nat. Nanotechnol.* **18**, 456–463 (2023).
11. Yu, H. et al. Wafer-scale growth and transfer of highly-oriented monolayer MoS_2 continuous films. *ACS Nano* **11**, 12001–12007 (2017).
12. Wang, Q. et al. Wafer-scale highly oriented monolayer MoS_2 with large domain sizes. *Nano Lett.* **20**, 7193–7199 (2020).
13. Li, L. et al. Epitaxy of wafer-scale single-crystal MoS_2 monolayer via buffer layer control. *Nat. Commun.* **15**, 1825 (2024).
14. Yu, H. et al. Eight in. wafer–scale epitaxial monolayer MoS_2. *Adv. Mater.* **36**, e2402855 (2024).
15. Li, T. et al. Epitaxial growth of wafer-scale molybdenum disulfide semiconductor single crystals on sapphire. *Nat. Nanotechnol.* **16**, 1201–1207 (2021).
16. Liu, L. et al. Uniform nucleation and epitaxy of bilayer molybdenum disulfide on sapphire. *Nature* **605**, 69–75 (2022).
17. Wang, Q. et al. Layer-by-layer epitaxy of multi-layer MoS_2 wafers. *Natl Sci. Rev.* **9**, nwac077 (2022).
18. Kang, K. et al. Layer-by-layer assembly of two-dimensional materials into wafer-scale heterostructures. *Nature* **550**, 229–233 (2017).
19. Quellmalz, A. et al. Large-area integration of two-dimensional materials and their heterostructures by wafer bonding. *Nat. Commun.* **12**, 917 (2021).
20. Christiansen, S. H., Singh, R. & Gosele, U. Wafer direct bonding: from advanced substrate engineering to future applications in micro/nanoelectronics. *Proc. IEEE* **94**, 2060–2106 (2006).
21. Alexe, M. & Gösele, U. *Wafer Bonding: Applications and Technology* (Springer, 2013).
22. Kim, J., Ju, X., Ang, K.-W. & Chi, D. Van der Waals layer transfer of 2D materials for monolithic 3D electronic system integration: review and outlook. *ACS Nano* **17**, 1831–1844 (2023).
23. Li, J. et al. Chemical vapor deposition of 4 inch wafer-scale monolayer $MoSe_2$. *Small Sci.* **2**, 2200062 (2022).
24. Na, S. R. et al. Selective mechanical transfer of graphene from seed copper foil using rate effects. *ACS Nano* **9**, 1325–1335 (2015).
25. Walker, E. S. et al. Large-area dry transfer of single-crystalline epitaxial bismuth thin films. *Nano Lett.* **16**, 6931–6938 (2016).
26. Hong, N. et al. Roll-to-roll dry transfer of large-scale graphene. *Adv. Mater.* **34**, 2106615 (2022).
27. Lin, Z. et al. Controllable growth of large–size crystalline MoS_2 and resist-free transfer assisted with a Cu thin film. *Sci. Rep.* **5**, 18596 (2016).
28. Cao, Z., Tao, L., Akinwande, D., Huang, R. & Liechti, K. M. Mixed-mode traction-separation relations between graphene and copper by blister tests. *Int. J. Solids Struct.* **84**, 147–159 (2016).
29. Hutchinson, J. W. & Suo, Z. Mixed mode cracking in layered materials. *Adv. Appl. Mech.* **29**, 63–191 (1991).

30. Wang, J.-S. & Suo, Z. Experimental determination of interfacial toughness curves using Brazil-nut-sandwiches. *Acta Metall. Mater.* **38**, 1279–1290 (1990).
31. Borges, C. et al. A strain rate dependent cohesive zone element for mode I modeling of the fracture behavior of adhesives. *Proc. Inst. Mech. Eng. Part L* **234**, 610–621 (2020).
32. Kang, S., Yoon, T., Kim, S. & Kim, T.-S. Role of crack deflection on rate dependent mechanical transfer of multilayer graphene and its application to transparent electrodes. *ACS Appl. Nano Mater.* **2**, 1980–1985 (2019).
33. Splendiani, A. et al. Emerging photoluminescence in monolayer MoS_2. *Nano Lett.* **10**, 1271–1275 (2010).
34. Lin, M.-L. et al. Moiré phonons in twisted bilayer MoS_2. *ACS Nano* **12**, 8770–8780 (2018).
35. Liu, K. et al. Evolution of interlayer coupling in twisted molybdenum disulfide bilayers. *Nat. Commun.* **5**, 4966 (2014).
36. Xin, K., Wang, X., Grove-Rasmussen, K. & Wei, Z. Twist-angle two-dimensional superlattices and their application in (opto) electronics. *J. Semicond.* **43**, 011001 (2022).
37. Du, L. et al. Moiré photonics and optoelectronics. *Science* **379**, eadg0014 (2023).
38. Shen, C. et al. Correlated states in twisted double bilayer graphene. *Nat. Phys.* **16**, 520–525 (2020).
39. Zhang, Z. et al. Flat bands in twisted bilayer transition metal dichalcogenides. *Nat. Phys.* **16**, 1093–1096 (2020).
40. Chubarov, M., Choudhury, T. H., Zhang, X. & Redwing, J. M. In-plane X-ray diffraction for characterization of monolayer and few-layer transition metal dichalcogenide films. *Nanotechnology* **29**, 055706 (2018).
41. Nguyen, V. L. et al. Wafer-scale integration of transition metal dichalcogenide field-effect transistors using adhesion lithography. *Nat. Electron.* **6**, 146–153 (2023).
42. Liu, J. et al. Direct bonding and debonding of two-dimensional semiconductors. *figshare* https://doi.org/10.6084/m9.figshare.30252058.v1 (2025).

Acknowledgements

We thank K. Liu and Y. Ye at Peking University for providing graphene and $MoTe_2$ samples, respectively, and X. He at Songshan Lake Materials Laboratory for LEED characterizations. This work is supported by the National Key Research and Development Program of China (Grant Nos. 2021YFA1202900 to G.Z., 2021YFA1400502 to D.S. and 2023YFA1407000 to L. Du), the National Science Foundation of China (Grant Nos. 62488201 to G.Z., 12422402 to L. Du, 12274447 to L. Du, 62204166 to N. Li and 62405205 to X.Z.), the Guangdong Major Project of Basic and Applied Basic Research (Grant No. 2021B0301030002 to G.Z.), the Strategic Priority Research Program of the Chinese Academy of Sciences (Grant No. XDB0470101 to D.S.) and the China National Postdoctoral Program for Innovative Talents (Grant No. BX20230251 to X.Z.).

Author contributions

G.Z. supervised this work. J.L. and J.Z. performed the wafer bonding and debonding experiments. L.L., Z.W., J.W.L., Q.W., L.Z. and H.Y. grew the monolayer MoS_2 and $MoSe_2$ wafers. T.L. fabricated and measured the devices. D.J. and L.D.X. performed the density functional theory calculations. J.L. performed the AFM, PFM and low wavenumber Raman characterizations. L. Dai performed the direct PL imaging. J.Z. performed the Raman mappings. M.Z. and J.L. performed the XRD measurements. H.S. performed the TEM characterizations. Y.L. and J.L. performed the SHG characterizations. J.L., J.Z., L. Du, W.Y., D.S., N. Li and G.Z. analysed the data. Y.C., F.W., S.Z., J.T., X.Z., N. Lu, X.B., Z.C., S.L. and S.W. contributed to discussions. J.L. and G.Z. wrote the paper with input from N. Li, L. Du and W.Y.

Competing interests

The authors declare no competing interests.

Additional information

Extended data is available for this paper at https://doi.org/10.1038/s41928-025-01474-3.

Supplementary information The online version contains supplementary material available at https://doi.org/10.1038/s41928-025-01474-3.

Correspondence and requests for materials should be addressed to Guangyu Zhang.

Peer review information *Nature Electronics* thanks Jianbin Xu, Ioanna Zergioti and the other, anonymous, reviewer(s) for their contribution to the peer review of this work.

https://doi.org/10.1038/s41928-025-01474-3

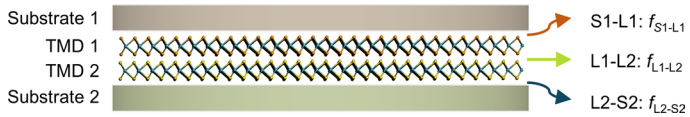

Extended Data Fig. 1 | The three van der Waals interfaces formed after wafer-bonding.

https://doi.org/10.1038/s41928-025-01474-3

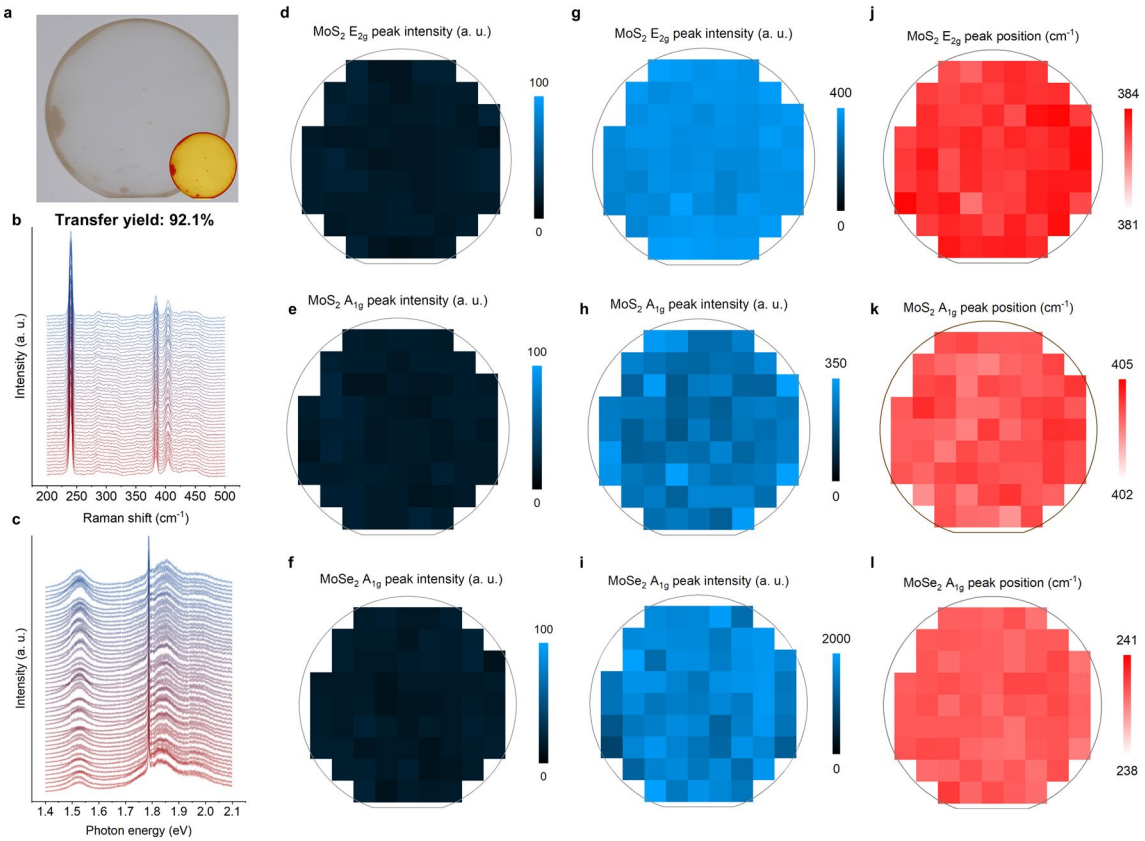

Extended Data Fig. 2 | Optical characterizations of as-fabricated $MoSe_2/MoS_2$ wafer. a, Photo of sapphire wafer after $MoSe_2$-exfoliation and contrast-enhanced version (inset) showing wafer-scale transfer yield of 92.1%. **b**–**c**, Representative Raman spectra (**b**) and photoluminescence (PL) spectra (**c**) at 50 different locations on the wafer. **d**–**f**, Raman intensity mapping of sapphire wafer after $MoSe_2$-exfoliation at MoS_2 E_{2g} peak (**d**), MoS_2 A_{1g} peak (**e**), and $MoSe_2$ A_{1g} peak (**f**). **g**–**i**, Raman intensity mapping of $MoSe_2/MoS_2$ wafer at MoS_2 E_{2g} peak (**g**), MoS_2 A_{1g} peak (**h**), and $MoSe_2$ A_{1g} peak (**i**). **j**–**l**, Raman peak position mapping of $MoSe_2/MoS_2$ wafer at MoS_2 E_{2g} peak (**j**), MoS_2 A_{1g} peak (**k**), and $MoSe_2$ A_{1g} peak (**l**).

https://doi.org/10.1038/s41928-025-01474-3

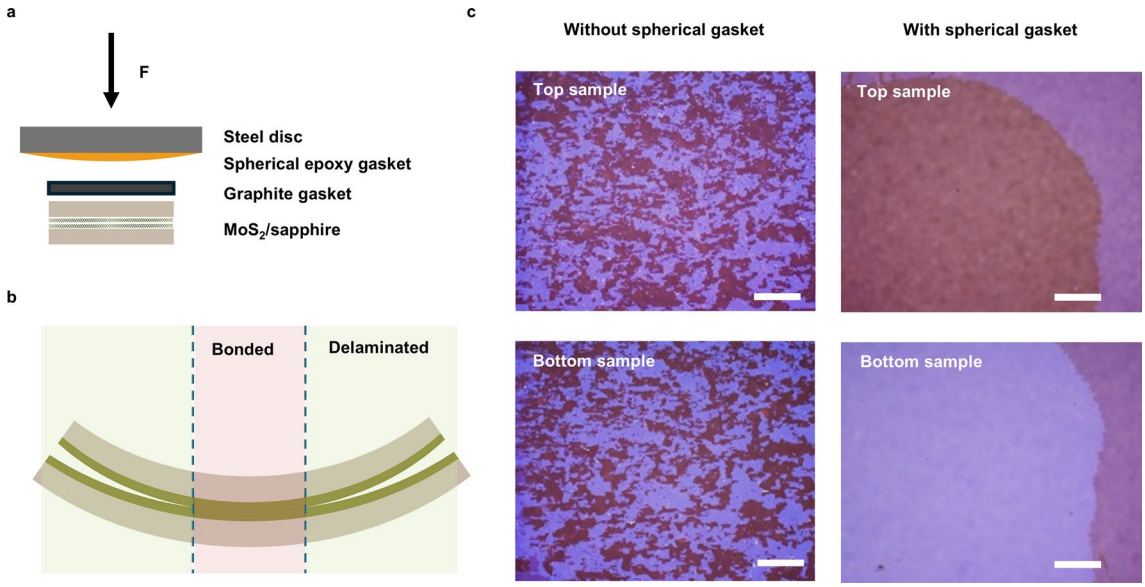

Extended Data Fig. 3 | Bonding-debonding of 2D materials with identical adhesion energy to their substrates. a, Illustration showing the setup of bonding-debonding with spherical epoxy gasket. **b**, Warped wafer pair after bonding with a slightly domed pressing head. **c**, Optical micrographs of top and bottom MoS_2 samples after bonding-debonding without (left column) and with (right column) the use of spherical epoxy gasket, scale bar: 300 µm.

https://doi.org/10.1038/s41928-025-01474-3

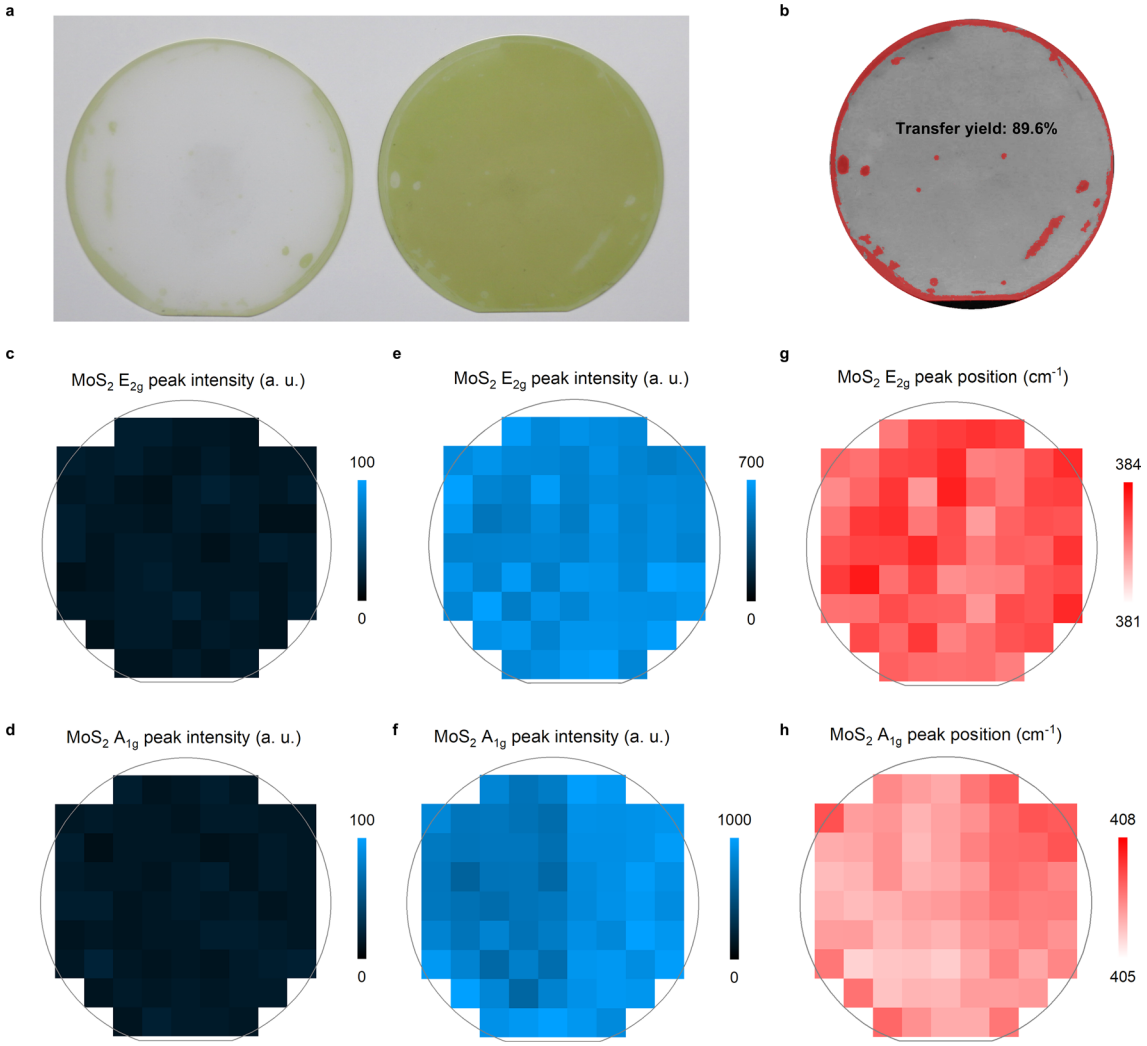

Extended Data Fig. 4 | Wafer-scale bonding-debonding fabrication of bilayer MoS_2 wafer. a, Photograph of sapphire wafer after MoS_2-exfoliation (left) and bilayer MoS_2 wafer (right). **b**, Contrast-enhanced photo of bilayer MoS_2 showing wafer-scale transfer yield of 89.6%. **c**–**d**, Raman intensity mapping of sapphire wafer after MoS_2-exfoliation at MoS_2 E_{2g} peak (**c**) and MoS_2 A_{1g} peak (**d**). **e**–**f**, Raman intensity mapping of bilayer MoS_2 wafer at MoS_2 E_{2g} peak (**e**) and MoS_2 A_{1g} peak (**f**). **g**–**h**, Raman peak position mapping of MoS_2 bilayer MoS_2 wafer at E_{2g} peak (**g**) and A_{1g} peak (**h**).

https://doi.org/10.1038/s41928-025-01474-3

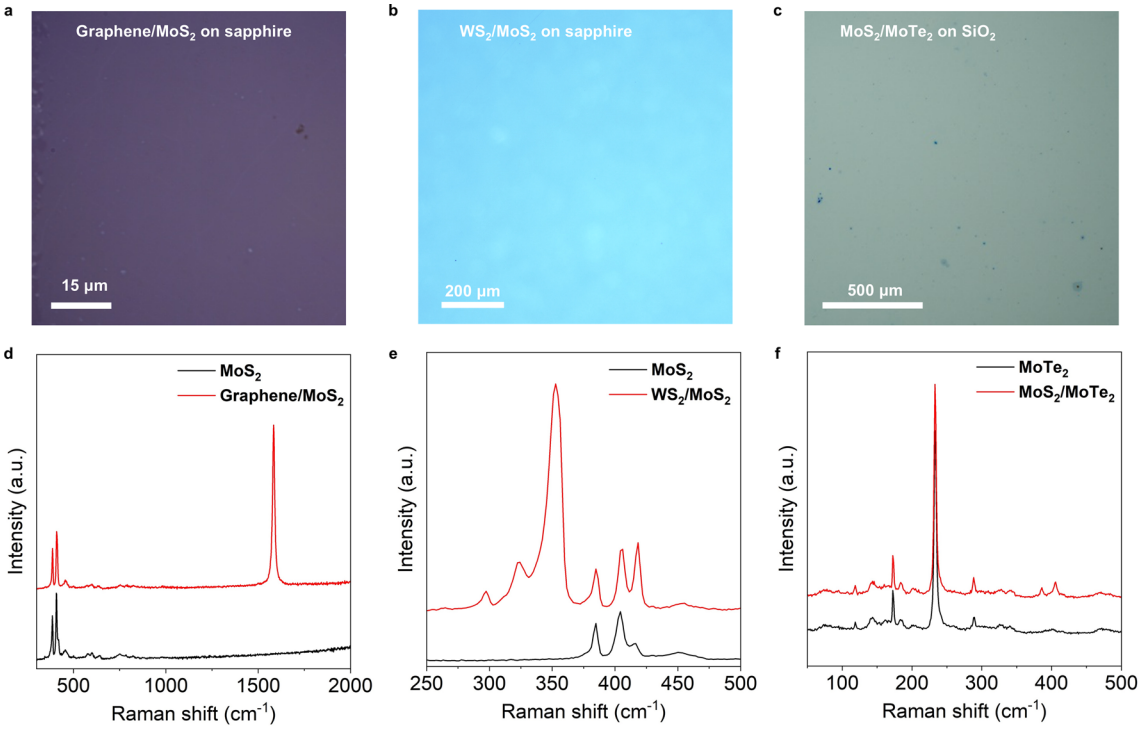

Extended Data Fig. 5 | Bonding-debonding technique applied to other 2D materials. a, Graphene/Cu foil transferred onto MoS_2/sapphire and corresponding Raman spectra (**d**). **b**, WS_2/sapphire transferred onto MoS_2/sapphire and corresponding Raman spectra (**e**). **c**, MoS_2/sapphire transferred onto $MoTe_2/SiO_2$ and corresponding Raman spectra (**f**).

https://doi.org/10.1038/s41928-025-01474-3

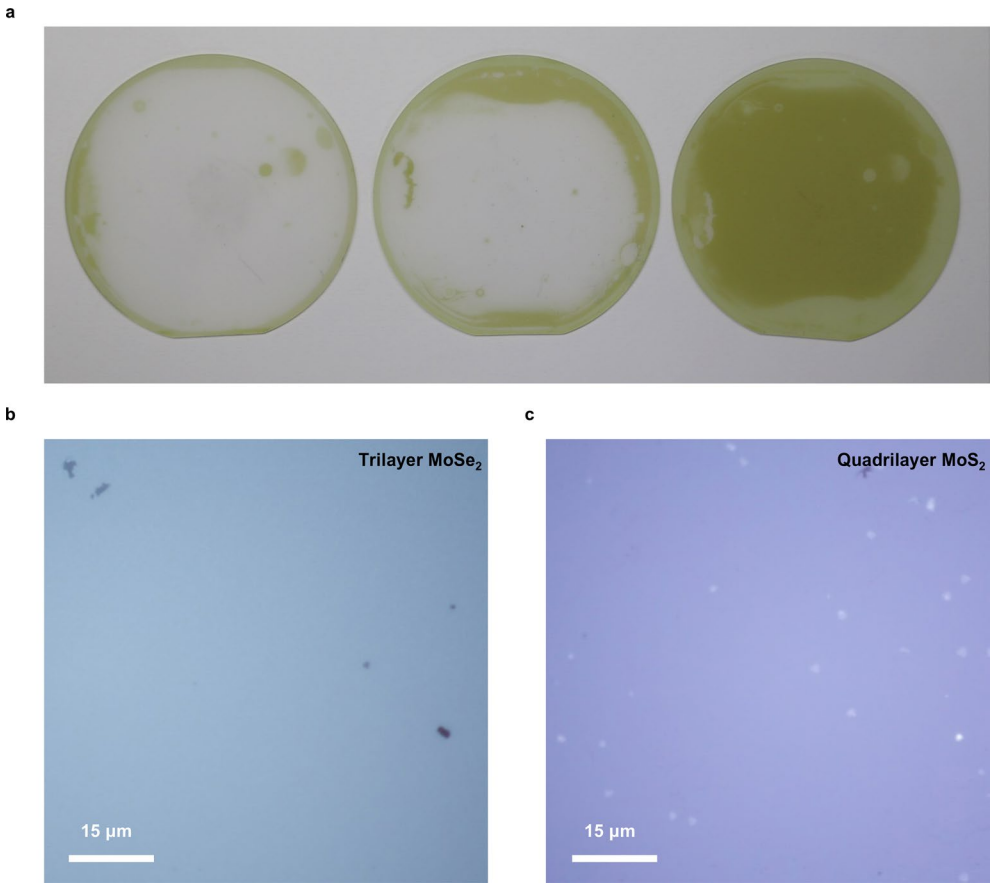

Extended Data Fig. 6 | Multilayer TMDs fabricated by bonding-debonding method. a, Photo of a 2-inch trilayer MoS_2 wafer after 2 consecutive bonding and debonding. **b**–**c**, Optical micrograph of trilayer $MoSe_2$(**b**) and quadrilayer MoS_2(**c**).

https://doi.org/10.1038/s41928-025-01474-3

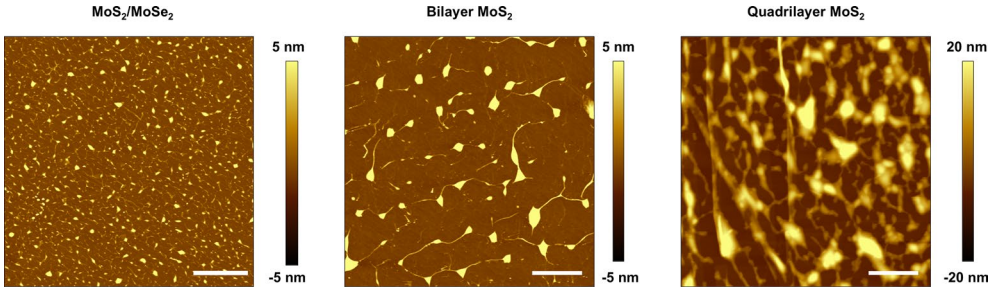

Extended Data Fig. 7 | AFM images of $MoSe_2/MoS_2$, bilayer MoS_2, and quadrilayer MoS_2 samples prepared by wet transfer. Left, AFM image of $MoSe_2/MoS_2$ prepared by wet transfer. Middle, AFM image of bilayer MoS_2 prepared by wet transfer. Right, AFM image of quadrilayer MoS_2 samples prepared by wet transfer.

https://doi.org/10.1038/s41928-025-01474-3

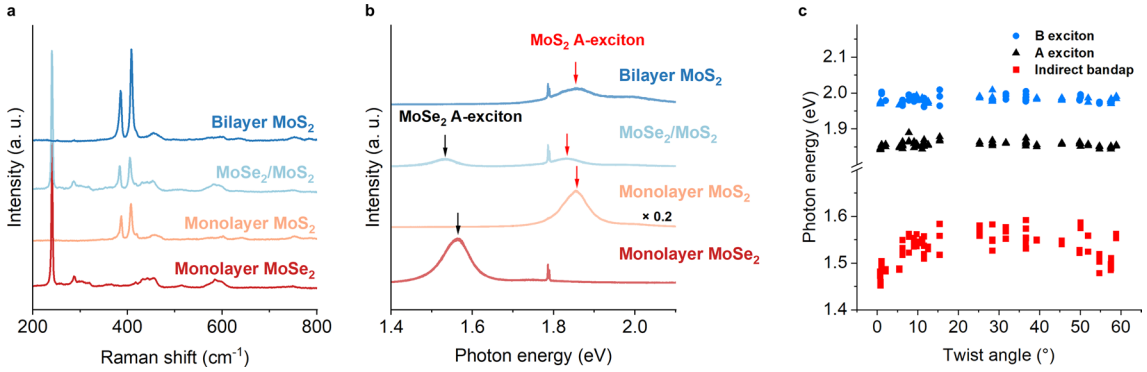

Extended Data Fig. 8 | Additional optical characterizations of as-fabricated films. a, Raman of spectra of monolayer $MoSe_2$, monolayer MoS_2, as-fabricated $MoSe_2/MoS_2$ and bilayer MoS_2. **b**, PL of spectra of monolayer $MoSe_2$, monolayer MoS_2, as-fabricated $MoSe_2/MoS_2$ and bilayer MoS_2, with highlighted MoS_2 A-exciton peak (red arrows) and $MoSe_2$ A-exciton peak (black arrows). **c**, Peak positions of A exciton, B exciton and indirect bandgap of twisted bilayer MoS_2 with different twist angles.

https://doi.org/10.1038/s41928-025-01474-3

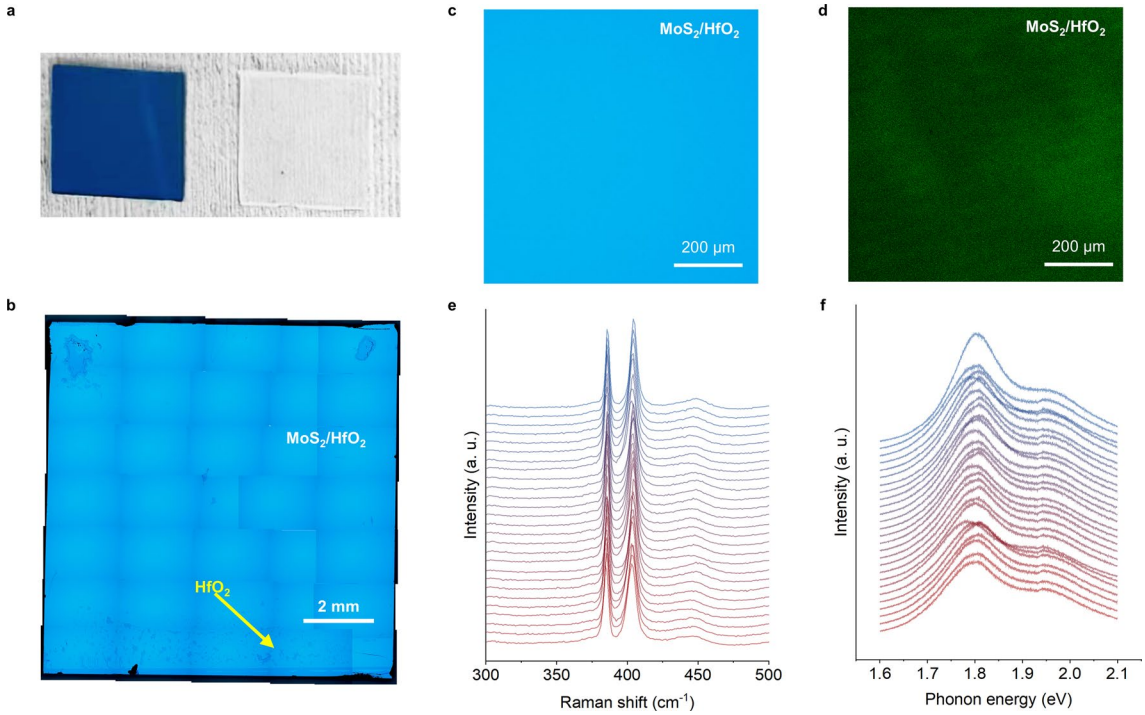

Extended Data Fig. 9 | Bonding-debonding transfer of MoS_2 onto HfO_2. **a**, Photograph of 1*1 cm^2 MoS_2/HfO_2 on SiO_2 (left) and bare sapphire substrate after MoS_2-exfoliation (right) by bonding-debonding. **b**, X5 microscopy images mapping of sample shown in (**a**). **c**, Single X5 microscopy image of sample shown in (**a**). **d**, Direct PL imaging of sample shown in (**a**). **e**–**f**, Representative (**e**) Raman spectra and (**f**) photoluminescence (PL) spectra at 27 different locations on sample in (**a**).

https://doi.org/10.1038/s41928-025-01474-3

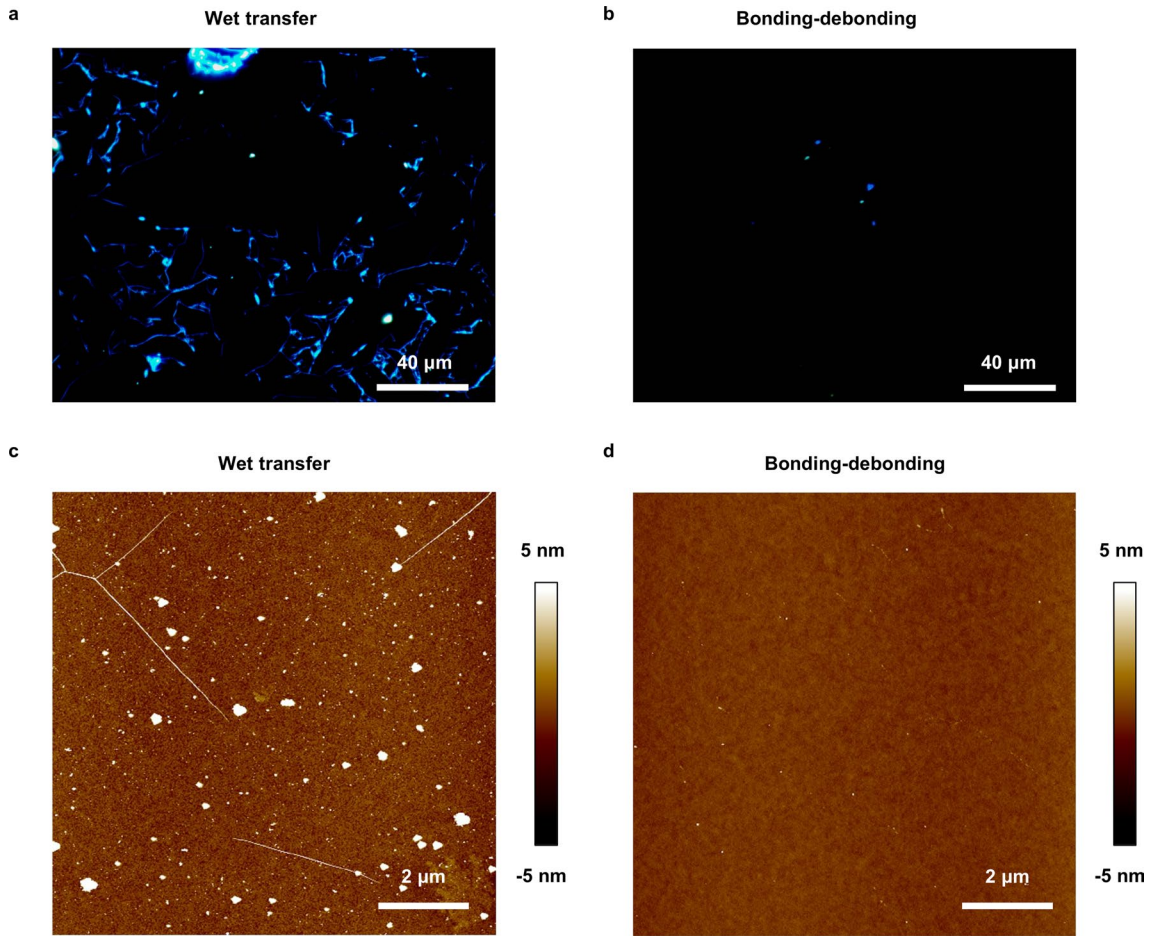

Extended Data Fig. 10 | Transfer MoS_2 film onto HfO_2 substrates by wet transfer and bonding-debonding. a–b, Dark-field microscopy images of MoS_2/HfO_2 by (**a**) wet transfer and (**b**) bonding-debonding. **c–d,** AFM images of MoS_2/HfO_2 samples by (**c**) wet transfer and (**d**) bonding-debonding.